Active Gravity compensation using Tendon Antagonism for Earth-based testing of Space Soft Continuum Robotics

MSc Thesis to obtain the degree of Master of Science Robotics

Arnout Dourleijn

4916832

Department of Cognitive Robotics
Delft University of Technology

Supervisor: Prof. Cosimo Della Santina

Daily Supervisor: Dr. Ebrahim Shahabi Shalghouni

Daily Supervisor: Dr. Daniel Feliu Talegón

February 2026

***Abstract*—Continuum soft manipulators (CSMs) offer key advantages over rigid robots for on-orbit servicing (OOS), but their deployment requires realistic ground-based testing environments. To emulate microgravity conditions for CSMs, this paper proposes tendon antagonism as a model-based gravity compensation method. It is shown that a tendon layout design consisting of one linear tendon and two tendons shaped as five-segment piecewise-linear approximations of sinusoids is sufficient to counteract planar bending moment by gravitational loading. Dynamic simulations compare a gravity-loaded plant model, a gravity-free reference model, and an uncompensated baseline using a geometric variable strain formulation. Results show accurate tracking on bending DOFs with negligible ($10^{-5}\ rad/m$) tracking errors in steady-state conditions and remain small during motion ($10^{-2}\ rad/m$), increasing moderately at higher actuation levels. Small errors in task space (18 mm) stem from uncontrolled elongation DOF, as tendon actuation is limited to tension only. The design is further validated experimentally, using machine vision for pose estimation. Results show high accuracy of the simulation, and demonstrate that tendon antagonism reduces gravitational sagging and enables tracking of the reference configuration across actuation values. Average positional error reduces by 80%, from 103 mm to 18 mm when using the compensation mechanism. At high actuation values, results show overcompensation for the gravity load, hinting to possible improvements in the tendon control scheme. Future research could implement real-time control or control of the remaining free DOFs.**

I. Introduction

Our cosmic backyard, low earth orbit (LEO), is getting full. The number of satellites launched per year is growing fast [1], and seventy years of spaceflight has littered (LEO) with debris, like spent rocket stages or defunct satellites. Satellites in orbit have to actively avoid collisions and a single collision in orbit can cause the creation of thousands more pieces of debris. NASA's orbital debris program estimates that there are approximately 500,000 marble-sized particles in orbit, all with enough kinetic energy to cause devastating damage [2]. Not taking action could in the worst case lead to the Kessler Syndrome, where a runaway chain reaction of collision could render LEO uninhabitable for any active satellite [3]. In-orbit servicing or active debris removal could help to keep LEO clear of uncontrollable objects, ensuring safe access to space for the future. Satellite servicing can extend operational lifetimes by repairing satellites or remove debris safely by capturing and deorbiting it in a controlled way. However, this is made difficult by the diversity of the objects in orbit and the variety of tasks needed. Most satellites are designed-for-purpose, often without in-orbit servicing in mind [4]. They can differ in size and shape, from CubeSats the size of a milk carton to giant space telescopes like Hubble the size of a bus. Moreover, most defunct space objects are tumbling: rotating about their own axes with various speeds. This makes grabbing them even more difficult.

Soft robotics offers significant advantages over conventional rigid robotics for on-orbit servicing (OOS) applications. Soft grippers exhibit high misalignment tolerance, soft capture, and passive compliance, outperforming rigid end-effectors in dexterous OOS missions [5]. Unlike rigid robots that rely primarily on end-effectors, soft continuum robots can use their entire body to wrap around targets, adapting to complex shapes due to their infinite degrees of freedom (DOFs) [6]. While no soft continuum robots have yet flown in space, the potential applications are substantial, with the OOS market expected to grow rapidly [7].

However, deploying soft robots in space introduces unique challenges. The microgravity environment significantly impacts robot design and control strategies [8]. Robot motion on a spacecraft induces disturbances that must be carefully modelled to minimize adverse effects on the vehicle and related systems [9]. Extreme temperatures, radiation, and the absence of gravity alter material behaviour and complicate design validation [10]. Paradoxically, reduced gravity presents a key advantage for continuum robots: their length and tip displacement are typically constrained under Earth's gravity due to low stiffness, but in microgravity, longer, more accurate, and dynamically capable robots become feasible [6]. On Earth, however, fully replicating the continuum robot's infinite DoFs in microgravity remains challenging. Traditional microgravity testing for rigid manipulators uses suspension rigs, counterweights, springs, airbeds or actuator-based gravity compensation [11], [12], [13], [14], [15], [16], [17], [18], [19]. Despite extensive literature on soft continuum robots and microgravity simulations, there is a clear research gap: no existing test setup fully compensates for gravitational effects in soft continuum robots designed for OOS in 3D space. Developing such a test setup is crucial for the future implementation of these systems in real OOS missions, as the space sector demands extremely high reliability and precision. Without representative terrestrial testing that accurately mimics microgravity conditions, the performance, safety, and controllability of soft continuum manipulators cannot be confidently validated prior to deployment. Addressing this gap is therefore a necessary step toward enabling safe, effective, and practical on-orbit servicing operations using soft continuum robotics.

The research presented here aims to bridge this gap. Following the literature research, four main avenues were investigated as conceptual solutions. Potential energy balancing via counterweights or springs is a method

often applied in conventional robotics, where the effects of gravity are balanced to ensure no change in potential energy over the robot's range of motion [20]. However, this was not deemed applicable to soft robots due to the infinite number of DOFs needed to balance. More specific to soft continuum robots, tendon antagonism, variable stiffness and high stiffness/weight ratio were investigated. A continuum robot with a very high stiffness to weight ratio is a very simple solution, as it will not show large effects caused by gravity. However, most soft continuum robots do not fall in this material range, and accepting this as a solution would exclude most of the most commonplace materials from the testing possibilities. Thus this concept was written off. Secondly, the possibilities of variable stiffness were investigated. Many different methods have been proposed in literature that allow for a continuum robot to exhibit changing levels of stiffness [21]. However, this alone could never fully compensate for the effect of gravity and would interfere with the normal actuation of the robot. This concept was also discarded. Finally, tendon antagonism remained as the most promising solution.

Thus, this research presents a novel design of a continuum soft manipulator (CSM) using tendon antagonism to offset gravitational loads, applicable to a simple 3-armed gripper. Using a combination of a linear and two sinusoidally shaped tendons, the gravity load is decomposed and compensated for. Due to the inherent limitations of the tendon actuation mechanism and the complexity of the system only the bending component is directly compensated. This is sufficient in practice, as bending generates the largest deflections along the manipulator and thus dominates the gravity-induced errors. Next to the mathematical model, a prototype CSM is built to validate its workings. Using this prototype, this report demonstrates the capability of tendon antagonism to compensate for the gravity load in a CSM in both static and dynamic cases.

II. Methodology

A. Mathematical Model

The CSM is modelled as a single, continuous Cosserat rod, a continuous sequence of rigid cross-sections parametrized by a material coordinate $X \in [0, L]$, where L is the total length of the rod. For simplicity, this parameter is often normalised as $s = X/L \in [0, 1]$. This continuous model was then discretised using the geometric variable strain (GVS) method [22], which extends the widely used piecewise-constant strain method and divides the rod into a finite set of strain basis functions. The following formulas summarize key functions and readers are referred to the original source for the complete mathematical details. By attaching a moving reference frame to each cross-section, the configuration of the rod is described by a curve $g : s \mapsto g(s) \in SE(3)$. The homogeneous transformation matrix representing this configuration is

$$\mathbf{g} = \begin{pmatrix} \mathbf{R} & \mathbf{r} \\ \mathbf{0}^T & 1 \end{pmatrix}, \tag{1}$$

where $R \in SO(3)$ is the rotation matrix and $r \in \mathbb{R}^3$ is the position vector. The partial derivatives with respect to space (denoted by $(\cdot)_0$) and time (denoted by $\dot{(\cdot)}$) are defined as

$$\mathbf{g}_0^i(s_i) = \mathbf{g}_i \, \boldsymbol{\xi}_{b_i}, \tag{2}$$

$$\dot{\mathbf{g}}_i(s_i) = \mathbf{g}_i \, \boldsymbol{\eta}_{b_i}^r, \tag{3}$$

where

$$\boldsymbol{\xi}_{b_i}(s_i) = \begin{bmatrix} \tilde{\mathbf{k}}_i & \mathbf{p}_i \\ \mathbf{0} & 0 \end{bmatrix} \in \mathfrak{se}(3), \quad \boldsymbol{\xi}_i(s_i) = \begin{bmatrix} \mathbf{k}_i \\ \mathbf{p}_i \end{bmatrix} \in \mathbb{R}^6, \tag{4}$$

defines the strain twist in the body frame and

$$\boldsymbol{\eta}_{b_i}^r(s_i) = \begin{bmatrix} \tilde{\mathbf{w}}_i^r & \mathbf{v}_i^r \\ \mathbf{0} & 0 \end{bmatrix} \in \mathfrak{se}(3), \quad \boldsymbol{\eta}_i^r(s_i) = \begin{bmatrix} \mathbf{w}_i^r \\ \mathbf{v}_i^r \end{bmatrix} \in \mathbb{R}^6, \tag{5}$$

is the velocity twist relative to the predecessor in the body frame. In (3), $\tilde{\mathbf{k}}_i(s) \in \mathfrak{so}(3)$, $\mathbf{k}_i(s) \in \mathbb{R}^3$, and $\mathbf{p}_i(s) \in \mathbb{R}^3$ are, respectively, the angular and linear strains. In (4), $\tilde{\mathbf{w}}_i^r(s) \in \mathfrak{so}(3)$, $\mathbf{w}_i^r(s) \in \mathbb{R}^3$, and $\mathbf{v}_i^r(s) \in \mathbb{R}^3$ are, respectively, the angular and linear velocity relative to the predecessor. The system is discretized and generalized coordinates are introduced by (6).

$$\boldsymbol{\xi}_i(s_i) = \mathbf{B}_{\xi_i} \mathbf{q}_i + \boldsymbol{\xi}_i^*, \tag{6}$$

where $\mathbf{B}_{\xi_i}(s_i) \in \mathbb{R}^{6 \times n_i}$ (n_i being the number of degrees of freedom (DoF) of link i) is a matrix function whose columns form the basis for the strain field, $\mathbf{q}_i \in \mathbb{R}^{n_i}$ is the vector of coordinates in that basis, and $\boldsymbol{\xi}_i^*(s_i) \in \mathbb{R}^6$ is a reference strain. In this paper, the CSM is assumed to be planar in the XZ plane. Shear deformation is assumed to be negligible. It was found that a 2nd order polynomial was sufficient to model the bending around the y-axis and normal strain was assumed to be constant. Thus, the basis matrix becomes

$$\mathbf{B}_{\xi_i}(s) = \begin{bmatrix} 0 & 0 & 0 & 0 \\ 1 & s & s^2 & 0 \\ 0 & 0 & 0 & 0 \\ 0 & 0 & 0 & 1 \\ 0 & 0 & 0 & 0 \\ 0 & 0 & 0 & 0 \end{bmatrix} \tag{7}$$

Using these generalised coordinates, the generalized dynamic equation can now be found to be

$$\mathbf{M}(\mathbf{q})\,\ddot{\mathbf{q}} + \mathbf{C}(\mathbf{q},\dot{\mathbf{q}})\,\dot{\mathbf{q}} + \mathbf{K}\,\mathbf{q} + \mathbf{D}\,\dot{\mathbf{q}} = \mathbf{B}(\mathbf{q})\,\mathbf{u} + \mathbf{F}(\mathbf{q},\dot{\mathbf{q}}) \tag{8}$$

In this formulation, $\mathbf{M}(\mathbf{q}) \in \mathbb{R}^{n\times n}$ denotes the mass matrix, while $\mathbf{C}(\mathbf{q},\dot{\mathbf{q}}) \in \mathbb{R}^{n\times n}$ represents the Coriolis matrix. The matrices $\mathbf{D} \in \mathbb{R}^{n\times n}$ and $\mathbf{K} \in \mathbb{R}^{n\times n}$ correspond to the system's damping and stiffness, respectively. Actuation is described by the matrix $\mathbf{B}(\mathbf{q}) \in \mathbb{R}^{n\times n_a}$ (see (10)), while $\mathbf{F}(\mathbf{q},\dot{\mathbf{q}}) \in \mathbb{R}^{n}$ collects the generalized external forces acting on the system. The applied actuation forces are given by the vector $\mathbf{u} \in \mathbb{R}^{n_a}$.

The effect of tendon actuation can be modelled as in (9) [22]. The tension is assumed to be constant across the tendon and working purely in the direction of the actuator path.

$$\mathcal{F}_a(s) = \sum_{k=1}^{n_a} \begin{bmatrix} \mathbf{d_k} \times \mathbf{t} \\ \mathbf{t_k} \end{bmatrix} u = \mathbf{B}_\tau \mathbf{u}, \tag{9}$$

In this context, $\mathbf{B}_\tau(\mathbf{q},s) \in \mathbb{R}^{6\times n_a}$ denotes the actuation matrix, while $\mathbf{d}_k(s) \in \mathbb{R}^3$ represents the distance vector from the rod midline to the k-th actuator. The vector $\mathbf{t}_k(\mathbf{q},s) \in \mathbb{R}^3$ is the unit tangent vector along the actuator path, and the applied actuation forces are collected in the vector $\mathbf{u} \in \mathbb{R}^{n_a}$. To transform the tendon force $\mathcal{F}_a(s)$ into the generalised coordinate frame and obtain the actuation matrix $\mathbf{B}(\mathbf{q})$, we multiply by the base matrix $\mathbf{B}_\xi$ and integrate over the length of the CSM as in (10).

$$\mathbf{B}(\mathbf{q}) = \int_0^L \mathbf{B}_\xi^\top \mathbf{B}_\tau \, ds \tag{10}$$

The gravity load is a distributed load over the entire length of the rod, with a magnitude dependent on the rod's cross-sectional area and density as in (11), where $\mathbf{f_g}$ is the vector of the direction of gravity in the global frame.

$$\mathcal{F}_g(s,\mathbf{q}) = \rho A(s)\mathbf{f}_g \tag{11}$$

To describe the effect on the generalised coordinates, again the load is integrated over the length of the arm, and rotated using the global Jacobian J which maps the generalised velocities to the global twist.

$$\mathbf{F}_g(\mathbf{q}) = \int_0^1 \boldsymbol{J}(s,\mathbf{q})^\top \mathcal{F}_g(s,\mathbf{q}) ds \tag{12}$$

The GVS model was modelled in Sorosim [22], an opensource package for Matlab. A visual of the model is given in Figure 1. A step-by-step description of how to generate and operate the Sorosim model is given in appendix A, along with the model parameters.

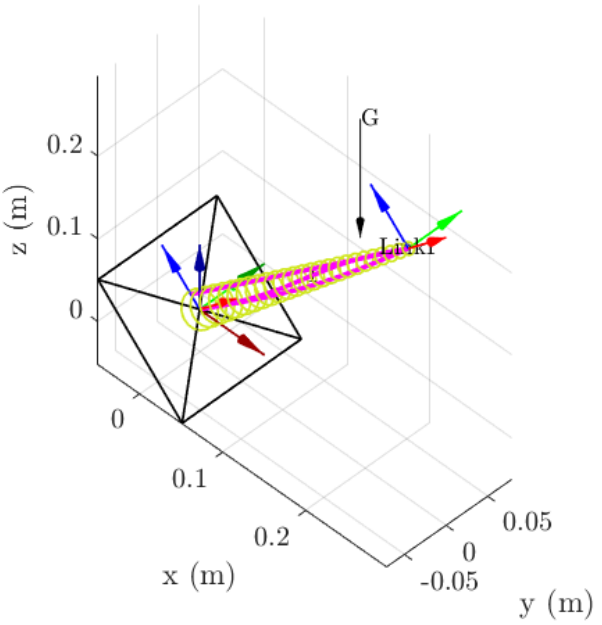

Fig. 1: Sorosim Linkage object showing the CSM (yellow rings) with three actuators (red dotted lines)

III. Tendon Antagonism

A. Operating Principles

The dynamics of the CSM are dictated by (8). Perfect gravity compensation would occur if the reference (no gravity, subscript r) and plant (with gravity, subscript p) configurations exactly coincide at any point in time:

$$\mathbf{q}_r = \mathbf{q}_p, \;\; \dot{\mathbf{q}}_r = \dot{\mathbf{q}}_p, \;\; \ddot{\mathbf{q}}_r = \ddot{\mathbf{q}}_p \tag{13}$$

with

$$\ddot{\mathbf{q}}_i = \mathbf{M_i}^{-1}(-\mathbf{C}\dot{\mathbf{q}}_i - \mathbf{K}\mathbf{q}_i - \mathbf{D}\dot{\mathbf{q}}_i + \mathbf{B}_i\mathbf{u}_i + \mathbf{F}_i) \tag{14}$$

wherein i is a placeholder for either p (plant) or r (reference). To simplify, $\boldsymbol{\tau}$ is defined as the sum of internal and Coriolis forces:

$$\boldsymbol{\tau} = \mathbf{C}\dot{\mathbf{q}} + \mathbf{K}\mathbf{q} + \mathbf{D}\dot{\mathbf{q}} \tag{15}$$

Simplifying (14) and substituting into (13) yields

$$\ddot{\mathbf{q}}_i = \mathbf{M}_i^{-1}(-\boldsymbol{\tau_i} + \mathbf{B}_i\mathbf{u}_i + \mathbf{F}_i) \tag{16}$$

$$\mathbf{M}_p^{-1}(-\boldsymbol{\tau}_p + \mathbf{B}_p\mathbf{u}_p + \mathbf{F}_p) = \mathbf{M}_r^{-1}(-\boldsymbol{\tau}_r + \mathbf{B}_r\mathbf{u}_r + \mathbf{F}_r) \tag{17}$$

Assuming that the gravity load does not influence the mechanical properties of the CSM, i.e. no geometric stiffening or non-linear deformations, the plant and reference share identical mass distribution and geometry. Consequently, the inertia mapping $\mathbf{M}$ is identical for both systems. In the ideal scenario, where (13 holds, the

same goes for $\boldsymbol{\tau}$. However, even small errors between the reference and plant configurations violate the ideal tracking assumption. Such deviations introduce additional forces due to stiffness, damping, and inertial effects. Especially in dynamical operation, a small offset in $\mathbf{q}$ will cause a growing error in the inertial and Coriolis matrices, requiring $\boldsymbol{\tau}$ to be included in the controller. It is further assumed that there are no external forces, except for gravity in the plant case ($\mathbf{F}_r = 0$). Thus, solving for the unknown tendon actuation term yields

$$\mathbf{B}_p\mathbf{u}_p = \boldsymbol{\tau}_p - \boldsymbol{\tau}_r + \mathbf{B}_r\mathbf{u}_r - \mathbf{F}_p \tag{18}$$

For this equation to hold $\mathbf{F}_g$ and $\mathbf{B}_r$ must lie in the span of the plant actuation matrix $\mathbf{B}_p$ and the rank of $\mathbf{B}_p$ must be equal to the degrees of freedom *n*. This is however not trivial. The gravity load is very complex and heavily dependent on the configuration $\mathbf{q}$. On the other hand, the choice of $\mathbf{B}_p$ and $\mathbf{u}_p$ are also not free, as they are limited by the physical nature of tendons and manufacturing limitations. The problem therefore becomes an optimization task in which the plant actuation matrix $\mathbf{B}_p$ must be designed such that its actuation input $\mathbf{u}_p$ minimizes the residual gravity load for any arbitrary configuration $\mathbf{q}$:

$$\min_{\mathbf{u}_p} \left\|\mathbf{B}_p\,\mathbf{u}_p + \mathbf{F}_p + \boldsymbol{\tau}_r - \boldsymbol{\tau}_p - \mathbf{B}_r\,\mathbf{u}_r\right\|. \tag{19}$$

B. Gravity decomposition

The gravity is modelled as in (11). The assumption is made that all parts in this equation vary smoothly over s, there are no jumps or discontinuities in A(s) or **J**(s). This assumption is only valid if the CSM is one continuous member with no hinges or discontinuities in shape. The dominant effect of gravity on the continuum soft manipulator is the bending moment. Consequently, the analysis focuses on this contribution. These assumptions allow for the bending moment in the body frame $m_g(s,\mathbf{q})$ to be modelled as a smooth, continuous curve over $s \in [0,1]$ for any value of $\mathbf{q}$. Consequently, $m_g(s,\mathbf{q})$ admits an expansion in a complete basis over this interval.

$$\phi_n(s) \in \{1,\ s,\ sin(n\pi s)\},\ n = 1,2,\ldots,\infty \tag{20}$$

$$m_g(s) = \sum_{n=0}^{\infty} c_n(\mathbf{q})\phi_n(s) \tag{21}$$

The set in (20) is selected which captures mean loading, first-order variation, and higher-order oscillatory contributions. Internal body mechanics dictate that the tip load is zero ($m_g(1,\mathbf{q}) = 0$), which implies that the cosine terms are not necessary and sine terms satisfy the boundary condition automatically. The constant and linear terms are included to capture offset and first-order variation across the backbone. The internal bending moment caused by gravity can therefore be written as (21) with configuration-dependent coefficients $c_k(\mathbf{q})$. This equation can be rewritten to matrix form

$$m_g(s,\mathbf{q}) = \mathbf{B}_m(s)\,\mathbf{u}_m(\mathbf{q}) \tag{22}$$

$$\mathbf{B}_m(s) = \begin{bmatrix}\phi_0(s) & \phi_1(s) & \ldots\end{bmatrix}, \quad \mathbf{u}_m(\mathbf{q}) = \begin{bmatrix}c_0(\mathbf{q})\\ c_1(\mathbf{q})\\ \vdots\end{bmatrix} \tag{23}$$

showing that using the infinite set as in (20), the gravity bending moment in the local frame can be rewritten to the form of $\mathbf{Bu}$, like in (9), showing the feasibility of decomposing the gravity bending moment into a linear combination of basis functions that can, in principle, be realized by appropriately routed tendon actuators.

C. Tendon basis

The goal of this section is to show that a set of physical tendon routings can generate actuator forces that span the same basis as the Fourier decomposition of the gravity bending moment. In other words, it is demonstrated that $\mathbf{B}_m\mathbf{u}_m$ can be realized with a combination of constant, linear, and sinusoidal tendons. Any planar tendon can be defined by a offset vector $\mathbf{d}(s)$ as in (24), describing the distance from the backbone at any point along s. The unit tangent vector can be found by taking the derivative of $\mathbf{d}(s)$ as in (25).

$$\mathbf{d}(s) = \begin{bmatrix}0\\0\\d(s)\end{bmatrix} \tag{24}$$

$$\hat{\mathbf{t}}(s) = \begin{bmatrix}dx\\dy\\dz\end{bmatrix} = \begin{bmatrix}1\\\frac{dy}{dx}\\\frac{dz}{dx}\end{bmatrix} = \begin{bmatrix}1\\0\\d(s)'\end{bmatrix} \tag{25}$$

$$\mathbf{t}(s) = \frac{1}{\sqrt{1+(d(s)')^2}}\begin{bmatrix}1\\0\\d(s)'\end{bmatrix} \tag{26}$$

The planar bending moment can then be found using (9) and simplified:

$$\mathbf{d}(s) \times \mathbf{t}(s) = \begin{bmatrix} 0 \\ 0 \\ d(s) \end{bmatrix} \times \frac{1}{\sqrt{1 + (d(s)')^2}} \begin{bmatrix} 1 \\ 0 \\ d(s)' \end{bmatrix} \tag{27}$$

$$\mathbf{d}(s) \times \mathbf{t}(\mathbf{s}) = \frac{1}{\sqrt{1 + (d(s)')^2}} \begin{bmatrix} 0 \\ d(s) \\ 0 \end{bmatrix} \tag{28}$$

The system is applied on a slender CSM where $d(s) \ll L$, where the assumption holds that the tendon remains nearly horizontal, i.e., $d'(s) \ll 1$, which is reasonable for shallow tendon slopes in typical CSM designs. Under this assumption, the cross product reduces to the tendon displacement itself, allowing a direct mapping between tendon shape and basis function, leading to the simplification of (27) to (29), where ϵ quantifies the deviation from the full cross-product expression. For sinusoidal tendon shapes, this error is negligible for lower-order harmonics but grows approximately quadratically with the harmonic number n, as higher-order modes produce steeper slopes along the backbone.

$$\mathbf{d}(s) \times \mathbf{t}(s) = \begin{bmatrix} 0 \\ d(s) + \epsilon \\ 0 \end{bmatrix} \tag{29}$$

As an example, Figure 2 shows the resulting bending moment term $d \times t$ from the tendon $d(s) = hsin(20\pi s)$ at three different length to height ratios h. It can be clearly seen that the horizontality assumption holds for $h = 0.01$ and $h = 0.005$, as the difference between the resulting bending moment and the tendon vector is small. However, as expected, at a higher length to height ratio bending moment term deviates significantly from the tendon vector $d(s)$. Figure 3 shows the mean absolute error between the tendon offset vector $d(s)$ and the resulting bending moment term $d \times t$ for a sinusoidal tendon with $d(s) = hsin(n\pi s)$ with $n \in [1, 2, \dots 20]$, again for the three values of h. The value of the error has been normalised with respect to h. It can be clearly seen that the error increases with period n and ratio h, as expected. It is thus shown that the assumption holds for low values of h and n, both of which are feasible when implementing tendons in a realistic CSM.

Table I summarizes the correspondence between the Fourier-like basis functions and the required tendon routings. This explicit mapping demonstrates that the tendon system spans the same functional space as the truncated Fourier expansion of $m_g(\mathbf{q})$ as in (21), but only in terms of bending moments along the backbone. Shear and axial forces are not independently controllable

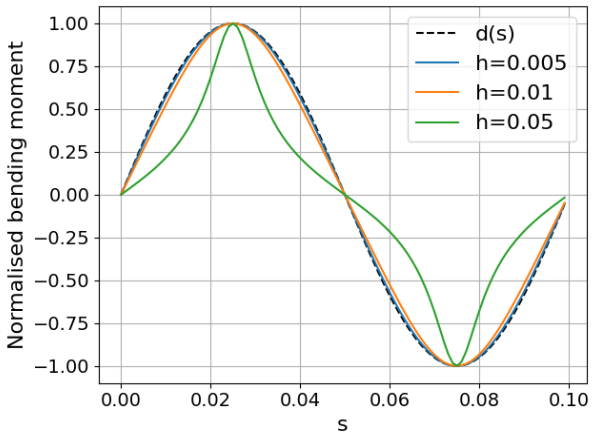

Fig. 2: Comparison of the normalised bending moment term $d \times t$ for three different length to height ratios h for $d(s) = hsin(20\pi s)$

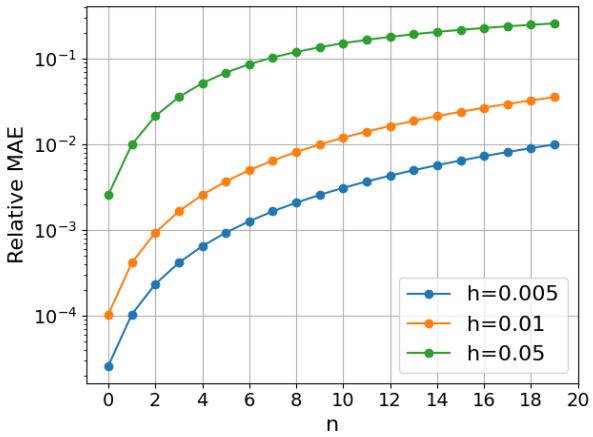

Fig. 3: Mean absolute error relative to h between $d(s) = hsin(n\pi s)$ and its resultant bending moment term $d \times t$ for three different length to height ratios h

by the tendon routing, and therefore the functional space generated by the tendons is restricted to the bending component. However, in this work their contribution to the CSM configuration is assumed to be negligible. Consequently, it is shown that the basis matrix $\mathbf{B}_m(s)$ in (22) can be constructed using a combination of linear and sinusoidal tendons, while the coefficient vector $\mathbf{u}_m(q)$ then defines, for any manipulator configuration $\mathbf{q}$, the set of tendon tensions required to realize the target gravity load.

IV. Final Design

A. Design Context

The CSM was designed with the explicit aim of being representative of standard CSM architectures reported

TABLE I: Tendon shapes corresponding to Fourier basis functions using the horizontality simplification.

Basis	$\mathbf{d}(s)$	$\hat{\mathbf{t}}$	$\mathbf{d}(s) \times \mathbf{t}(s)$
1	b	$\begin{bmatrix}1\\0\end{bmatrix}$	b
s	as	$\begin{bmatrix}1\\a\end{bmatrix}$	$\approx as$
$s+1$	as + b	$\begin{bmatrix}1\\a\end{bmatrix}$	$\approx as+b$
$sin(n\pi s)$	$bsin(n\pi s)$	$\begin{bmatrix}1\\bn\pi cos(n\pi s)\end{bmatrix}$	$\approx b\sin(n\pi s)$

in the literature. Its design parameters were additionally defined based on planned future testing and integration within DLR's on-ground simulation facility for on-orbit servicing operations (OOS-SIM) [23], as well as on practical manufacturing and laboratory constraints. The DLR OOS-SIM is capable of manipulating objects with dimensions of 25 × 25 × 25 cm; accordingly, the CSM was scaled to enable grasping objects of this size with a length of 0.380 meters. For the body material Dragon Skin™ 20 silicon rubber [24] was used. This material was selected due to its moderate stiffness (100% modulus of 0.33 MPa) and its widespread use in CSM design, making it representative of commonly employed elastomers. For simplicity, the CSM is only actuated for bending in one plane, with lateral bending and twisting remaining uncontrolled. This makes the prototype only capable of a simple grasping motion. The CSM is fixed to a 3D printed base, with three Dynamixel XM430-210-R motors which actuate the tendons. The motors operate in position-control mode, regulating the length of each tendon. This differs from the GVS model, where tendon tension is controlled directly. In this approach, the required tendon lengths are computed at each timestep using the GVS model. The physical CSM can then replay this simulated motion by following the recorded tendon length trajectories.

Next to theoretical efficiency, real-life applicability was also taken into account for the final design of the tendon antagonism system. When lying in a plane, tendons cannot cross. This limits the routing options of the tendons, especially when applying sinusoidal shapes with periods of less than s. To reduce complexity, it was decided to limit the amount of tendons to three. This proved sufficient to control the CSM as shown in the following chapters. The three tendons lie in the local xz-plane, with the z offset from the backbone in millimetres given by (30). The value of the 'amplitude' of the tendons was chosen as the largest possible without interference between any of the tendons and while lying fully within the CSM.

$$z_1 = 15 * (1 - s) \tag{30a}$$
$$z_2 = -7.5sin(\pi s) \tag{30b}$$
$$z_3 = -3.5sin(2\pi s) \tag{30c}$$

However, the fabrication of tendons perfectly following sinusoidal path was deemed implausible. During the potting of the tendons in the silicon rod, they can only be supported at a handful of discrete points, called linkages. These linkages are small plastic disks embedded in the arm, which hold the tendons in place. Between the linkages, pretension determines the path, which becomes (nearly) a straight line. To ensure any prototype would match with the model, the tendons were modelled as a discrete straight line interpolation of (30) at 5 points spaced equally over the arm lengths. This is the smallest number of sections that can still accurately approximate a sine with a period of the arm length. (31) shows the offset of the three final tendons at $s = [0\ 0.25\ 0.5\ 0.75\ 1]$ in millimeters. Figure 4 shows these tendons in the CSM.

$$d_1 = [15\ 11.3\ 7.5\ 3.8\ 0] \tag{31a}$$
$$d_2 = [0\ -5.3\ -7.5\ -5.3\ 0] \tag{31b}$$
$$d_3 = [0\ -3.5\ 0\ 3.5\ 0] \tag{31c}$$

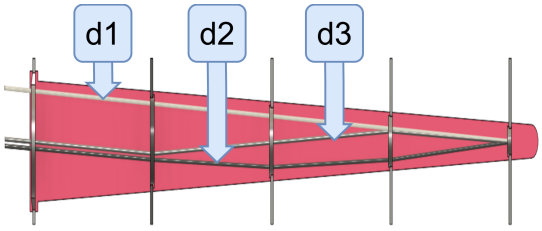

Fig. 4: Schematic overview (not at scale) of the final tendon design with the rod itself shown in pink and the internal tendons in gray

The CSM was also designed to be modular, allowing it to be configured as a three-armed soft robotic prototype gripper suitable for object manipulation for future testing. Figure 5 shows the full CAD model of the prototype gripper as an example of possible implementation of CSMs in the space industry.

B. Feed Forward Controller

To reproduce the reference configuration, a model-based feedforward law is implemented under a quasi-static

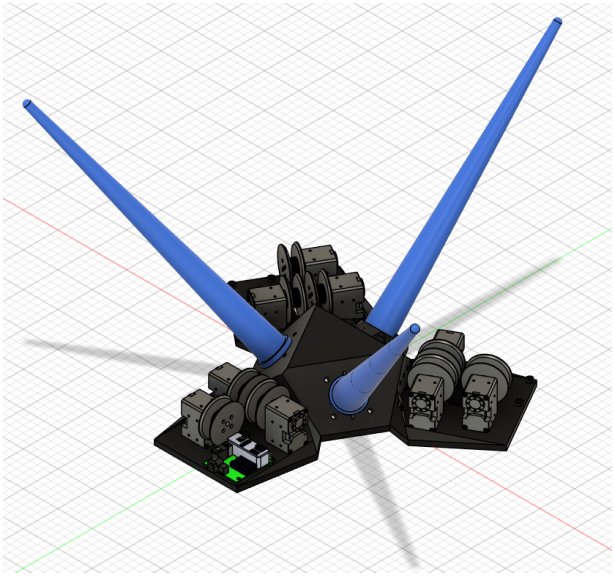

Fig. 5: 3D CAD model of the full gripper with 3 CSMs

assumption which generates the value of tendon actuation $\mathbf{u}_p$ for any configuration. The controller operates directly in configuration space. Rather than performing full inverse dynamics, the controller matches generalized forces, between the reference and plant models as in (18). For this, the controller requires complete knowledge of both the reference and plant CSM state at all times, including all loads. Since the controller's objective is to reproduce a specific time-varying configuration of the reference CSM, operating directly in configuration space reduces the number of required transformations without sacrificing accuracy. The GVS model can represent complex bending shapes with only a few degrees of freedom, enabling the controller to generate these curves far more efficiently than approaches that track multiple points along the rod in task space. Thus, the actuation is obtained by matching the generalized internal force vectors of the reference and plant models as

$$\mathbf{u_p} = \mathbf{B}_p^{-1}(\tau_p - \tau_r + \mathbf{B_r u_r} - \mathbf{F}_g) \tag{32}$$

where subscript *r* refers to the reference CSM, while subscript *p* refers to the plant model. To solve for $\mathbf{u}_p$, $\mathbf{B}_p$ must be invertible and thus wide: the number of DOFs that can be constrained is equal to the number of actuators in the system. As given in (7), the system is modelled with four discrete degrees of freedom, three for bending and one for extension. However, as described above, the system is controlled by only three actuators. By controlling only on the bending DOFs, the system becomes solvable. This can be achieved by projecting the system dynamics into the actuation subspace. This does mean that the extension DOF is not controlled.

C. Fabrication process

The CSM is cast in place in a 3D printed 2-piece mold, which holds the linkages and tendons in place and constrains the outer geometry. The mold is designed to be printed vertically, to reduce the visibility of the 3D printer's layering. One end of the mold remains open, so to allow silicon to be poured in. The first step of fabrication is to route the tendons through soft silicon tubes with a outer diameter of 2mm. These tubes allow the tendons to be decoupled from the silicon and move freely, massively reducing friction. The tendons are then routed through five linkages, which hold the tendons in place. A knot at the end ensures the tendons are securely fastened. The mold with tendons installed is shown in appendix B, Figure 20. To keep the tendons straight between the linkages, the tendons are pretensioned by fixing them to the mold. The linkages feature temporary fixture bars at the top and bottom, which allow them to be fixed inside the mold. After fabrication, these bars are easily broken off at their base due to a weakpoint.

With the tendons and linkages installed in the mold, the next step is the casting of the silicon. After mixing the 2 components equally by weight and volume, red dye is added to give the silicone its colour. The mixture is then degassed in a vacuum chamber for ten minutes to remove trapped air and reduce the number of bubbles, leading to a more homogenous result. After degassing, the silicon can be poured into the mold and is allowed to cure for several hours. Two methods of pouring were used: all at once or in two halves. Pouring the entire CSM requires the mold to be closed immediately. This means that the tendons cannot be seen or repositioned during pouring. It was found that some shifting of the tendons during casting is likely due to the high viscosity of the silicon mixture, even though the tendons are pretensioned. To remedy this, later designs were cast in two halves. By first casting the bottom half only, the tendons can be seen and, if necessary, repositioned during casting. Only once they are set in place, the mold is closed and the rest of the CSM is cast. After hardening, the CSM can be removed from the mold, the linkage bars can be broken off and any excess silicone can be trimmed to obtain the final result, shown in Figure 6. The prototype gripper is shown in Figure 7. Further testing of the full gripper design is relegated to future work.

V. Model Results

This chapter evaluates how accurately the plant model can compensate for the gravity load using the tendon antagonism method and reproduces a prescribed reference

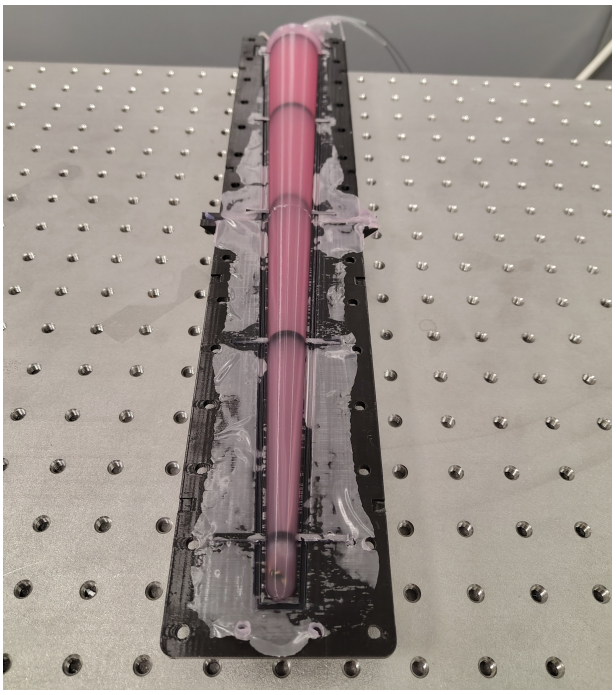

Fig. 6: Opened mold after hardening showing the CSM before postprocessing

Fig. 7: Full gripper prototype

trajectory generated by a reference model in the GVS simulation.

To quantify the working of the solution, the evolution of the values of the four DOFs of the CSM over time are investigated for different actuations of the reference arm. The reference arm is actuated solely with the linear tendon according to

$$\mathbf{u}_r(t) = \begin{cases} [0,0,0]^T, & \text{if } t \leq 1 \\ [u_r,0,0]^T, & \text{if } t > 1 \end{cases} \tag{33}$$

with $0 \leq u_r \leq 8N$ at an interval of $0.5N$. For example, Figure 8 shows the evolution of the DOFs for both reference and plant model where $u_r = 2N$. The DOFs refer to the values of $\mathbf{q}$, which is linked to the CSM's deformation via (6) and (7). As expected, the controller is able to closely follow the reference trajectory in the first three bending DOFs, but in doing so causes a large error in the elongation DOF. It is shown that the plant is able to accurately replicate the dynamical behaviour in the three bending degrees of freedom.

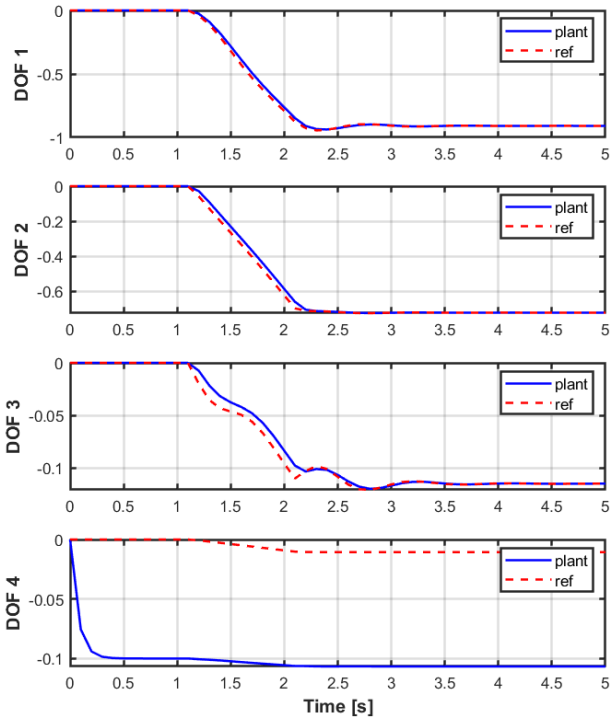

Fig. 8: Evolution of the 4 DOFs of the system in the plant (blue) and reference (red dotted) model

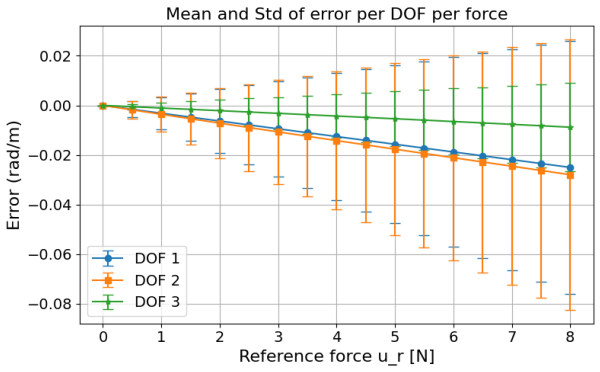

Fig. 9: Mean and standard deviation of error between $\mathbf{q}_p$ and $\mathbf{q}_r$ for the three bending DOFs over the entire movement

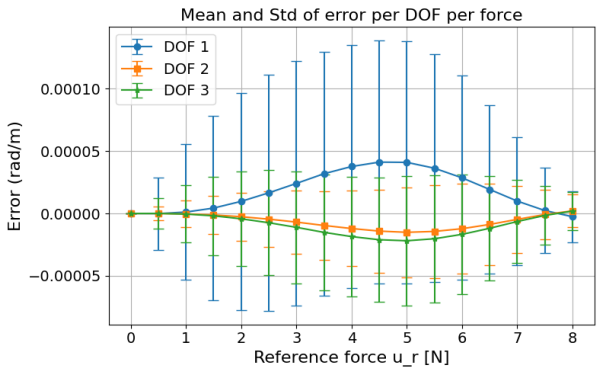

Fig. 10: Mean and standard deviation of error between $\mathbf{q}_p$ and $\mathbf{q}_r$ for the three bending DOFs for the static solution (last second)

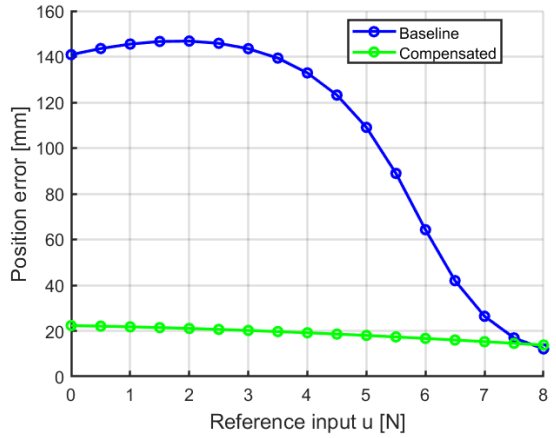

Fig. 11: Mean absolute position error along the CSM at the linkages, averaged over the full simulation time.

Figure 9 and Figure 10 show the tracking error between the reference state $\mathbf{q}_r$ and the plant state $\mathbf{q_p}$ for the full range of u_r, for the three bending degrees of freedom. In Figure 9, the error is shown over the full simulation ($0 \leq t \leq 5$ s), while Figure 10 focuses on the steady state, i.e., the last second of the simulation. Across all cases, the error is small relative to the typical magnitude of the DOFs (0.1–1). In the steady state, the error is on the order of 10^{-5}, effectively negligible. During the dynamic portion of the simulation, the error increases to approximately 10^{-2} but remains small, consistent with the trends shown in Figure 8. It can also be observed that the error grows slightly with higher actuation levels. This indicates that tracking errors are larger during faster motions, while they are negligible under static or quasi-static conditions. Figure 12 shows a simulation of three CSMs subjected to the same actuation pattern as above ($u_r = 2N$). The red rod represents the reference CSM, loaded purely by the linear actuator. The blue rod is the baseline CSM, loaded with gravity in addition to the reference actuation. The green rod represents the plant CSM, also loaded with gravity, but controlled using the tendon antagonism system with the feedforward controller to follow the reference. At $t = 0$, all rods are identical. Between $t = 0$ and $t = 1$, gravity causes the baseline and plant CSMs to be loaded downward. The baseline rod quickly sags under its own weight, while the plant is able to compensate and remains straight. Tendon tension induces compression, causing the plant rod to shrink. After $t = 1$, the reference rod begins to move, and the plant closely follows it. The baseline cannot overcome its weight and remains bent downward. Since the plant is actively controlled on its bending DOFs, the bending strains of the plant and baseline rods are nearly identical. However, differences in elongation result in the plant exhibiting a tighter curvature than the baseline CSM. To compare performance in task space quantitatively, Figure 11 shows the average position offset in space between the reference model and either the plant or baseline model for the four linkages in the CSM. The error is shown for all levels of reference actuation and is averaged over time over the entire simulation. It can be seen that the mean position error of the plant model is consistent at around 20 mm across the full actuation range. The mean error of the baseline is more variable, with high errors of around 150 mm at low actuation values ($u_r \leq 4.5N$) but decreasing to 20 mm at $u_r = 8N$. Thus the gravity compensation can be clearly seen to significantly reduce the position error, particularly for smaller actuation values.

VI. Experimental Validation

In order to validate the simulation, the behaviour of the system was tested experimentally for a single CSM. The CSM pose was measured using a monocular vision system based on ArUco fiducial markers (DICT_4X4_50) implemented in OpenCV (Python). Five 15 mm markers were rigidly attached to the linkage segments. Image data were acquired using a Logitech BRIO (V-U0040) camera at 1920×1080 resolution and 10 Hz via the Microsoft Media Foundation backend. The camera was calibrated using a standard checkerboard procedure and marker poses were estimated using OpenCV's *estimatePoseSingleMarkers* routine. For each configuration, poses were recorded for one second and temporally averaged to reduce measurement noise. Figure 13 shows the testing setup with the CSM in pink. The pose estimation of these markers in the camera frame can be seen overlaid on the markers. The marker pose at the base was used to align camera and model frame.

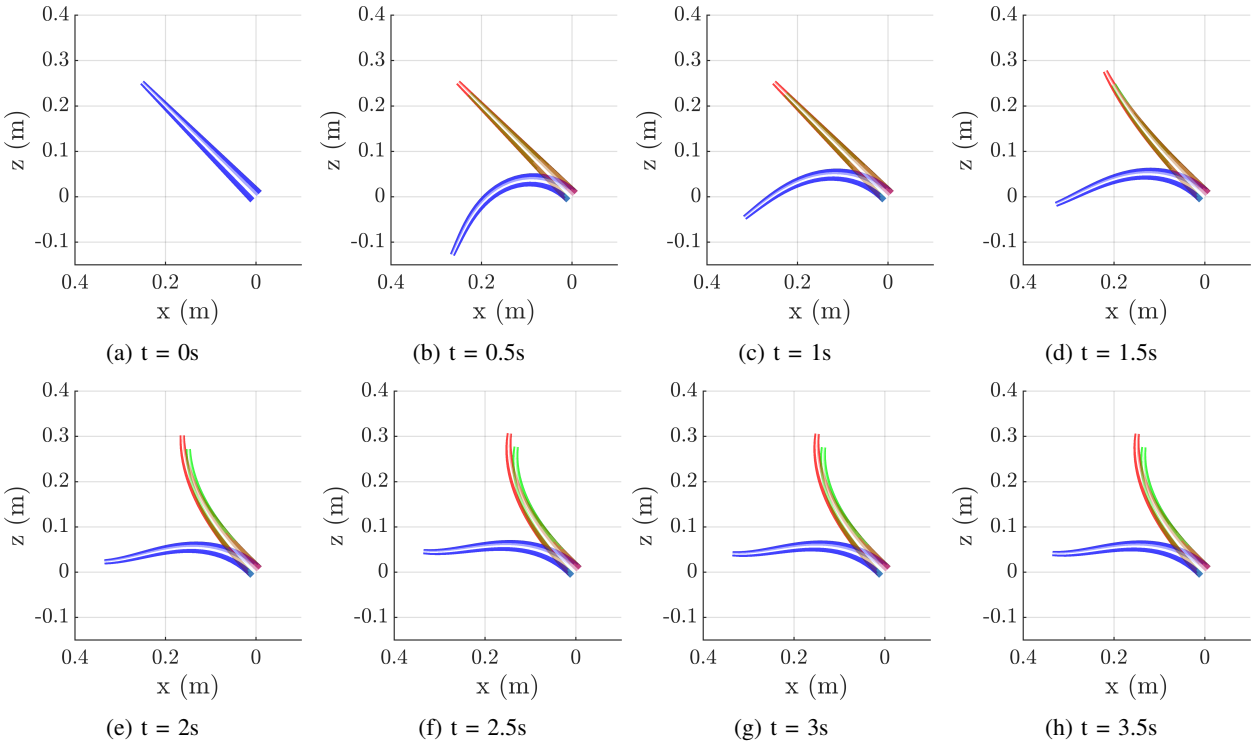

(a) t = 0s (b) t = 0.5s (c) t = 1s (d) t = 1.5s

(e) t = 2s (f) t = 2.5s (g) t = 3s (h) t = 3.5s

Fig. 12: Dynamic model of the CSM in reference (No gravity, red), baseline (gravity, no compensation, blue) and plant (gravity, compensated, green) over 3.5 seconds for $u_r = 2N$

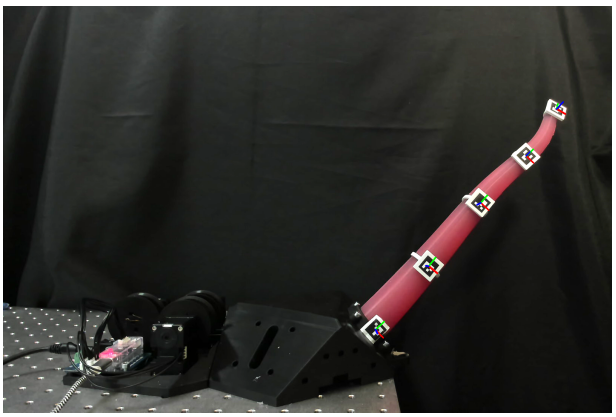

Fig. 13: Snapshot from the machine vision model, with the prototype CSM in 'straight' configuration. The tracking of the 5 ArUco markers is visible.

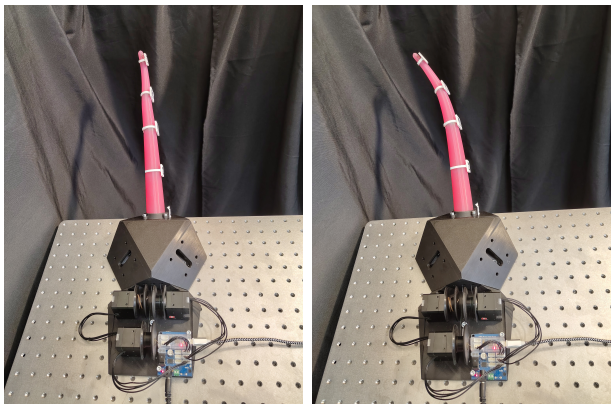

(a) With lateral guidance (b) Without lateral guidance

Fig. 14: Top view of the demonstrator CSM showing lateral bending

During the experiments, a consistent lateral bending of the arm was observed, caused by production defects induced out-of-plane deformation that is not captured by the planar assumptions of the model. Figure 14 shows a top view, where the lateral bending is clearly visible in the right pane. However, it is possible to keep the system straight by manually enforcing a straight starting position, as in Figure 14a. This is done by moving the tip of the CSM back into the XZ plane by hand after boot up. Two experimental conditions are therefore evaluated: (i) the natural system behaviour including erroneous lateral bending, and (ii) a constrained configuration in which this deformation is manually suppressed to isolate the accuracy of the model-based control approach.

The model and the plant are compared at the steady state situation, because of difficulties in synchronising model

movement and recording. Figure 15 shows the position of the linkages in the XZ plane for both the model (red) and the measured demonstrator for reference actuation (blue) and with active gravity compensation $u_r = 0\ N$ and $u_r = 8\ N$ with (green) and without (purple) the manual lateral guidance. The shown positions are the average of 5 trials to reduce the effect of measurement noise. In Figure 15a it can be seen that the last linkage for the uncompensated measurement is missing, due to excessive rotation making the marker invisible. However, both measurements show that the arm comes close to the desired straight shape, showing a small offset approaching a second harmonic sinus. In Figure 15b the errors have increased. The demonstrator has bent less than expected in the model.

Figure 16 shows the positional error in the XZ plane between the reference model and either the baseline or plant, guided or unguided, measurements, averaged over the four linkages in the CSM. All data show very similar behaviour as in the model shown in Figure 11. At the lower actuation values, the data for the unguided variant is missing, again due to the lost tracking of the top marker. The error varies between 22 mm at $u_r = 1.5N$ and 14 mm at $u_r = 6N$. The difference between the unguided and guided measurements is small, with a maximum of 3 mm. To better compare the guided and unguided measurements, Figure 17 shows the same error data with the top link removed for fairer comparison. As expected the error decreases over all actuations to 16-10 mm, as the top marker deflects the most. The difference between the two measurements is still small, with the largest difference at low actuation values.

Table II summarizes the data shown in Figure 11 and Figure 16. The behaviour in simulation and experimental data is highly consistent. In both cases, the baseline model exhibits large errors at low actuation values that decrease as u_r increases, whereas the compensated case remains nearly constant over the full range. The mean errors are also nearly identical between simulation and measurement for both baseline (104 mm) and compensated cases (18–19 mm), indicating good model fidelity. The compensated error is effectively constant with respect to actuation. Across all u_r, it remains within a narrow band of approximately 14–22 mm in both simulation and measurements, demonstrating that the compensation largely removes the actuation-dependent bias present in the baseline case. Gravity compensation reduces the position error for almost the entire actuation range. The improvement is most pronounced at low actuation levels, where the baseline error exceeds 140 mm, while the compensated error remains around 20 mm.

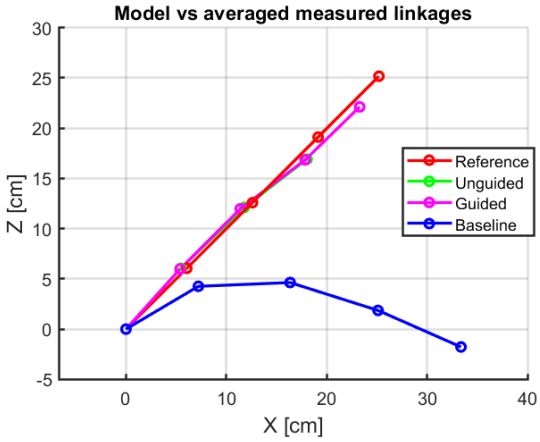

(a) $u_r = 0\ N$

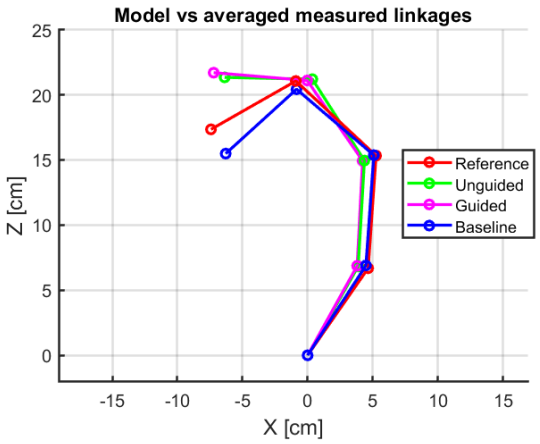

(b) $u_r = 8\ N$

Fig. 15: Comparison of the linkage positions in the X-Z plane between the GVS model reference (red), the uncompensated demonstrator (blue) and the demonstrator with gravity compensation with (purple) and without (green) manual lateral guidance for the minimum and maximum value of u_r

VII. Discussion

The presented results demonstrate that tendon antagonism combined with the proposed feedforward controller is effective in compensating gravitational loading and reproducing reference bending trajectories in a continuum soft manipulator. In the GVS simulation the plant model closely tracks the reference model in the three bending degrees of freedom, across all tested actuation levels. In static conditions, errors were in the order of 10^{-5} with fairly constant values across a reference actuations. In dynamic simulations the errors increase to 10^{-2}, showing a linear correspondence with the actuation magnitude. This increase can be attributed

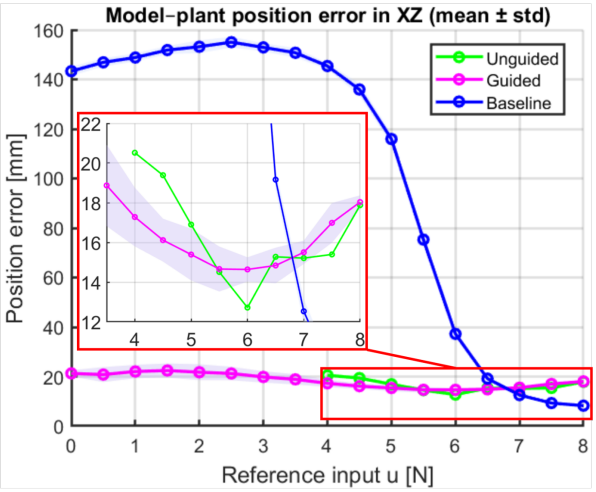

Fig. 16: Average linkage position error to simulation reference in the XZ plane across all linkages for all u_r including baseline measurement. Missing data at $u_r < 4N$ is caused by failed tracking of last linkage marker at lower actuations.

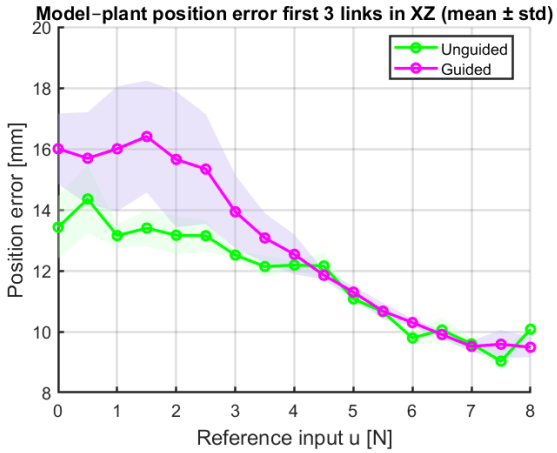

Fig. 17: Average linkage position error in the XZ plane across all u_r with the last linkage omitted.

to modelled dynamic effects, including inertial forces dependent on configuration $\mathbf{q}$ and coupling with the uncontrolled degrees of freedom. Larger actuation inputs lead to faster motions and higher internal forces, amplifying the influence of dynamic modelling inaccuracies. Nevertheless, the magnitude of the error remains low, suggesting that the model captures the dominant system dynamics sufficiently well for open-loop gravity compensation and moderate-speed motion.

Performance in task space was also investigated, for both the simulation as a real-life demonstrator. Simulations and measurements for the baseline case, where gravity

TABLE II: Quantitative comparison of average position error in mm in XZ plane to reference simulation at SS.

	Simulation		Measured		
$\mathbf{u_r}$[N]	Baseline	Plant.	Baseline	Guided	Unguided
0.0	141	22	143	21	NaN
0.5	144	22	147	21	NaN
1.0	146	22	149	22	NaN
1.5	147	21	152	22	NaN
2.0	147	21	153	22	NaN
2.5	146	21	155	21	NaN
3.0	143	20	153	20	NaN
3.5	139	20	151	19	NaN
4.0	133	19	145	17	21
4.5	123	19	136	16	19
5.0	109	18	116	15	17
5.5	89	17	75	15	15
6.0	64	17	37	15	13
6.5	42	16	19	15	15
7.0	26	15	13	16	15
7.5	17	15	9	17	15
8.0	12	14	8	18	18
Mean	**103.98**	**18.73**	**103.62**	**18.33**	**16.42**

remains uncompensated for, show very similar results with an average position error of 103.98 and 103.62 mm respectively as given in Table II. This shows that the simulations accurately captures real life behaviour of the CSM. As can be seen in Figure 11 and Figure 16, the data shows two main cases, depending on which load is the dominant factor in determining the deformation of the CSM: gravity or actuation. In the investigated design, this switch happens at around $u_r = 6N$. In the case that gravity is the dominant load, the difference between the baseline and reference model is naturally much larger then in the case where the actuation load is dominating. The measurements of the system with gravity compensation, in Figure 16 show a near constant error between 14 and 22 mm over the actuation range. This implies a decrease of 80% in the range of gravity domination. However, for actuation values of $u_r > 6.5N$, the position error of the baseline is actually lower than that of the gravity compensated CSM. Figure 15b shows the linkages' position in this case. It can be seen that the system has overcompensated for the effect of gravity and overshot the reference. This implies a increasing error in the linear tendon length control, which is to be expected at larger curvatures. Increasing the accuracy of this system or switching to direct force control could improve performance of the system at higher actuation.

The results show deformations in two undesired degrees of freedom: elongation and lateral bending. The behaviour in the elongation DOF is expected and directly results from the system being underactuated: only the three bending DOFs are actively controlled, while the axial DOF is left free. The tendon forces required to generate bending moments introduce axial compression,

which alters the rod length and therefore the curvature distribution. This highlights a fundamental flaw when using antagonistic tendons for shape control. Full compensation would require an actuator working on this degree of freedom. The effect of lateral bending on the in-plane bending is most apparent at lower actuation levels, where the difference between guided and unguided measurements reaches up to 3 mm. At higher actuation levels, the in-plane bending dominates the overall deformation, reducing the relative influence of lateral offsets. This shows that the effect of lateral freedom on the CSM's vertical bending is small. This lateral bending occurs because of small fabrication errors, causing the tendons to not lie exactly in the vertical plane. This offset causes a lateral bending and twisting moment, which cannot be compensated for with the current tendon configuration. This moment causes a slight offset, which causes the gravity load to exert a lateral bending/ twisting moment as well. Since balancing against gravity is an unstable equilibrium these small errors will quickly grow. The system shows high sensitivity to initial conditions. Addressing this limitation requires either the introduction of active lateral control or an increase in structural stiffness in the lateral direction through mechanical design changes.

VIII. Conclusion

This work proposes the use of tendon antagonism as a method for gravity compensation in a continuum soft manipulator (CSM). A geometric variable strain model was employed to model the CSM behaviour. It was shown that the bending moment resulting from the gravity load can be deconstructed in a linear part plus a set of sines. A tendon configuration was proposed featuring one linearly decreasing tendon and two linear approximations of sinuses with periods of one and two rod lengths. A feedforward controller operating in configuration space was implemented to generate the tendon actuation required to reproduce reference trajectories while counteracting gravitational loading. The approach was evaluated using a dynamic model of the manipulator and compared against both a gravity-free reference model and an uncompensated baseline model. The model was experimentally validated using a 0.38 meter CSM and machine vision-based marker tracking.

Gravitational deflection, which causes significant sagging in the baseline model, is effectively compensated in the controlled plant. While compression induced by tendon tension leads to deviations in the elongation degree of freedom, this behaviour is consistent with the underactuated nature of the system and the mechanical coupling between bending and axial strain. Tracking errors remain very small in steady-state conditions and increase moderately during motion, particularly at higher actuation levels. Experimental validation shows small errors in the bending plane, but substantial lateral deflections. Despite these lateral offsets, the primary in-plane gravitational compensation is effective, and the CSM closely follows the intended bending trajectories. The results therefore demonstrate that tendon antagonism is a viable and efficient strategy for reducing gravitational effects in continuum soft manipulators.

Future work should focus on implementing real-time control, possibly integrating feedback to improve robustness against modelling uncertainties and disturbances, as well as control of the extension DOF and suppression of the lateral bending. Extending the method to more complex loading scenarios, integration in full microgravity setups and multi-arm manipulation tasks also represents a promising direction for further research.

References

[1] OECD, *The Space Economy in Figures: How Space Contributes to the Global Economy*. Paris: Organisation for Economic Co-operation and Development, 2023. [Online]. Available: https://www.oecd-ilibrary.org/economics/the-space-economy-in-figures_9789264307452-en

[2] NASA Orbital Debris Program Office, "Orbital debris program office," https://orbitaldebris.jsc.nasa.gov/, 2025, accessed: 2025-09-08.

[3] M. Shan, J. Guo, and E. Gill, "Review and comparison of active space debris capturing and removal methods," *Progress in aerospace sciences*, vol. 80, pp. 18–32, 2016.

[4] E. Papadopoulos, F. Aghili, O. Ma, and R. Lampariello, "Robotic manipulation and capture in space: A survey," *Frontiers in Robotics and AI*, vol. 8, p. 686723, 2021.

[5] B. Ma, Z. Jiang, Y. Liu, and Z. Xie, "Advances in space robots for on-orbit servicing: A comprehensive review," *Advanced Intelligent Systems*, vol. 5, no. 8, p. 2200397, 2023.

[6] M. Russo, "Continuum robots for space applications," in *International Conference on Robots for Space Applications in Orbital Stations*. Springer, 2023, pp. 129–139.

[7] V. Mate and L. Katare, "On-orbit satellite servicing market size, share, competitive landscape and trend analysis report by service, by orbit type, by end-user: Global opportunity analysis and industry forecast, 2023–2032," https://www.alliedmarketresearch.com/on-orbit-satellite-servicing-market, 2024, accessed: 2025-09-12.

[8] A. Flores-Abad, O. Ma, K. Pham, and S. Ulrich, "A review of space robotics technologies for on-orbit servicing," *Progress in aerospace sciences*, vol. 68, pp. 1–26, 2014.

[9] B. Weber, R. Balachandran, C. Riecke, F. Stulp, and M. Stelzer, "Teleoperating robots from the international space station: Microgravity effects on performance with force feedback," in *2019 IEEE/RSJ International Conference on Intelligent Robots and Systems (IROS)*. IEEE, 2019, pp. 8144–8150.

[10] Y. Zhang, P. Li, J. Quan, L. Li, G. Zhang, and D. Zhou, "Progress, challenges, and prospects of soft robotics for space applications," *Advanced Intelligent Systems*, vol. 5, no. 3, p. 2200071, 2023.

[11] R. Tanimoto, A. Moore, D. MacDonald, S. Thomas, A. Murray, O. Polanco, and G. Agnes, "Model and test validation of gravity offload system," in *48th AIAA/ASME/ASCE/AHS/ASC Structures, Structural Dynamics, and Materials Conference*, 2007, p. 1790.

[12] Y. Sato, A. Ejiri, Y. Iida, S. Kanda, T. Maruyama, T. Uchiyama, and H. Fujii, "Micro-g emulation system using constant-tension suspension for a space manipulator," in *Proceedings. 1991 IEEE International Conference on Robotics and Automation*. IEEE Computer Society, 1991, pp. 1893–1894.

[13] O. Han, D. Kienholz, P. Janzen, and S. Kidney, "Gravity-off-loading system for large-displacement ground testing of spacecraft mechanisms," in *Proceedings of the 40th aerospace mechanisms symposium*, 2010.

[14] H. B. Brown and J. M. Dolan, "A novel gravity compensation system for space robots," 1994.

[15] R. Zhou, Y. Zhou, X. Chen, W. Hou, C. Wang, H. Wang, and W. Jiang, "Gravity compensation method via magnetic quasi-zero stiffness combined with a quasi-zero deformation control strategy," *Science China Technological Sciences*, vol. 65, no. 8, pp. 1738–1748, 2022.

[16] C. Sullivan, K. Gebhardt, C. Solis, T. Mitchell, and N. A. Pehrson, "Accurate microgravity simulation for deployable structures," in *AIAA SCITECH 2023 Forum*, 2023, p. 1885.

[17] T. J. Bihl, K. D. Pham, and T. W. Murphey, "Modeling and control of active gravity off-loading for deployable space structures," in *Sensors and Systems for Space Applications*, vol. 6555. SPIE, 2007, pp. 337–346.

[18] V. Arakelian, "Gravity compensation in robotics," *Advanced robotics*, vol. 30, no. 2, pp. 79–96, 2016.

[19] Y. Fan, B. Yi, and D. Liu, "An overview of stiffening approaches for continuum robots," *Robotics and Computer-Integrated Manufacturing*, vol. 90, p. 102811, 2024.

[20] V. L. Nguyen, "Passive gravity compensation in mechanisms and robots: Methods, advances, and challenges," *Mechanism and Machine Theory*, vol. 220, p. 106345, 2026.

[21] D. Huang, L. Yang, and Y. Sun, "Variable stiffness of continuum robotics: A review," in *International Conference on Intelligent Robotics and Applications*. Springer, 2024, pp. 429–441.

[22] A. T. Mathew, I. B. Hmida, C. Armanini, F. Boyer, and F. Renda, "SoRoSim: A MATLAB toolbox for hybrid rigid–soft robots based on the geometric variable–strain approach," *IEEE Robotics & Automation Magazine*, vol. 30, no. 3, pp. 106–122, 2023.

[23] J. Artigas, M. De Stefano, W. Rackl, R. Lampariello, B. Brunner, W. Bertleff, R. Burger, O. Porges, A. Giordano, C. Borst *et al.*, "The oos-sim: An on-ground simulation facility for on-orbit servicing robotic operations," in *2015 IEEE International Conference on Robotics and Automation (ICRA)*. IEEE, 2015, pp. 2854–2860.

[24] Smooth-On, Inc. (2026) Dragon skin™ 20 silicone rubber. https://www.smooth-on.com/products/dragon-skin-20/. Smooth-On, Inc. Accessed: 2026-02-08. [Online]. Available: https://www.smooth-on.com/products/dragon-skin-20/

[25] Robotis, "Dynamixel xm430-w210-t/r e-manual," https://emanual.robotis.com/docs/en/dxl/x/xm430-w210/, Robotis, 2026, accessed: 2026-02-10.

APPENDIX

A. Sorosim Model

First a SorosimLink object is created which holds the physical parameters of the deformable member. The parameters are given in Table III.

```
Link = SorosimLink;
```

TABLE III: Parameters of the Sorosim Link object

Parameter	Value	Unit
E	425000	Pa
L	0.356	m
CS	C	
jointtype	N	
ρ	1080	g/cm^3
r_{start}	18.2	mm
r_{end}	5.8	mm

This link object is transformed into a SorosimLinkage object, where the free degrees of freedom are defined, as well as the actuators and placement in 3D space.

```
Linkage = SorosimLinkage(Link);
```

The link is placed at the origin with a $\alpha = -0.785\ rad$ angle around the y-axis, to match the prototype gripper. The deformable degrees of freedom are defined as 2nd order bending around the y-axis and 0th order extension. 11 Gaussian interpolation points are applied, to ensure sufficient accuracy for the tendon length calculation. No independent chain joints are applied, gravity is applied in the negative z direction and no point wrenches are applied. The number of actuators is selected as three. The first actuator is linear and can thus be created in the GUI by choosing the 'oblique' option, and selecting 0.015 as starting z-offset, zero for all other coordinates, and starting/end division as 1. For the remaining two actuators, 'None' is chosen as path type, as their unconventional shape has to be applied using a script by modifying the *dc* and *dcp* variables of the SorosimLinkage object. These variables hold the tendon offset and its derivative at all significant points along the rod's centerline. Once the Linkage creation is complete, a simulation can be run, outputting a time vector and the linkage's DOF's and their derivatives.

```
[t, qqd] = Linkage.Dynamics;
```

To apply custom control, a controller can be applied in *CustomActuatorInput.m*, which generates tendon action based on the state *qqd*. The *Linkage.CAI* parameter has to be set to 1 for this controller to be used in the simulation.

The tendon lengths are calculated using a custom script called *tendonlengths.m*, using as input the *qqd* vector at both start and end state. Using the linkage's forward kinematics function, the location and rotation of all

significant points in space can be found. At each of these points, the tendons can be added by rotating the *dc* vector and adding that to the significant point's position vector. Calculating the linear distance between these points gives the length of the tendon. The difference between the start (deformed under gravity) and end point gives the amount of actuation send to the motors.

B. Gripper Design

As described in subsection IV-A, the CSM's was designed with future integration into DLR's OOS-SIM testing set-up in mind as a three manipulator gripper. This determined general design parameters like CSM length, radius and base angle. Figure 18 shows the CAD model of the completed gripper, consisting of three CSM's, mounted on a hexagonal base at a 45° angle to the horizontal plane, each actuated by three Dynamixel XM430-210-R servomotors. These motors were chosen for their low cost, high torque, high reliability and ease of use. Their parameters are given in Table IV. The base features a modular design, allowing for the easy (de)installation of CSM's, motors, or even whole motor sub-assemblies. The base is made from 3D printed PLA, as it is not expected to bear any large loads or to have to operate in extreme conditions. Provisions have been made to mount it to a table featuring a 25 x 25mm m6 grid. The CSM's are secured to the base using a 3D printed ring. It is placed around the base of CSM, allowing it to be pressed against the base. It also features small cutouts so the rotation of the CSM can be locked using the first internal linkage, and a flat surface for ArUco marker mounting. The tendons pass through a slot in the base to enter the main cavity. Then on the opposite side, the tendons exit the cavity towards the motors. Each assembly features three motors, one for each tendon. There is one control board mounted on the gripper, which provides power and converts the RS-485 communication to USB. One board can power all 9 motors of the gripper, by daisy-chaining them.

TABLE IV: Motor Specifications (Dynamixel XM430-210-R) [25]

Parameter	**Specifications**
Position Sensor	Contactless absolute encoder (12-bit, 360°)
Resolution	4096 pulses/rev
Backlash	15 arcmin (0.25°)
Operating Modes	Current Control Mode Velocity Control Mode Position Control Mode (0 360°) Extended Position Control Mode (Multi-turn) Current-based Position Control Mode PWM Control Mode (Voltage Control Mode)
Gear Ratio	212.6 : 1
Stall Torque	3.0 N·m (12.0 V, 2.3 A)
Radial Load	40 N (10 mm from horn)
Axial Load	20 N

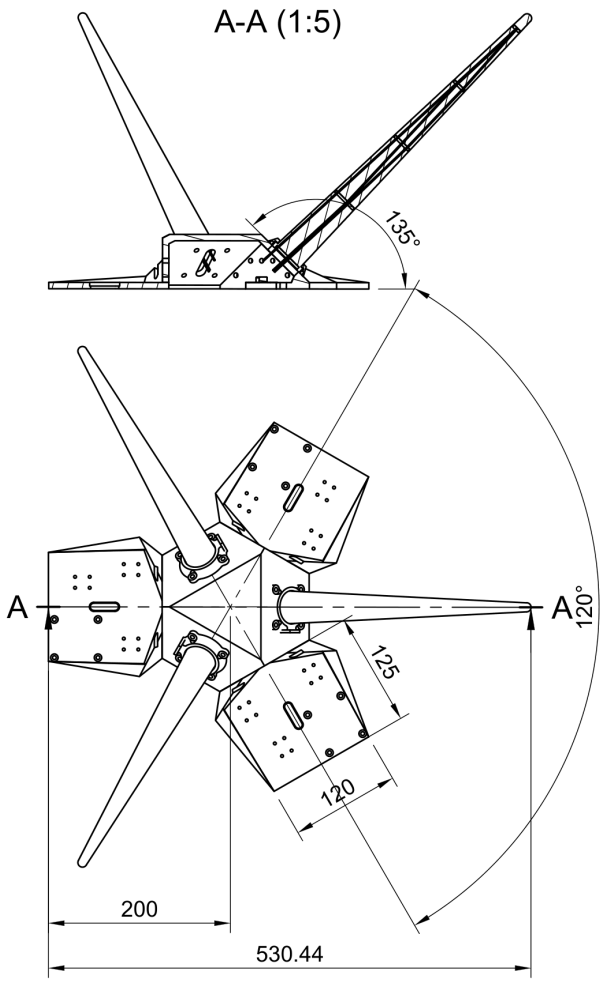

Fig. 18: Schematic of the full gripper design

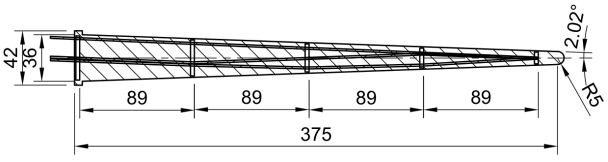

Fig. 19: Schematic of the CSM

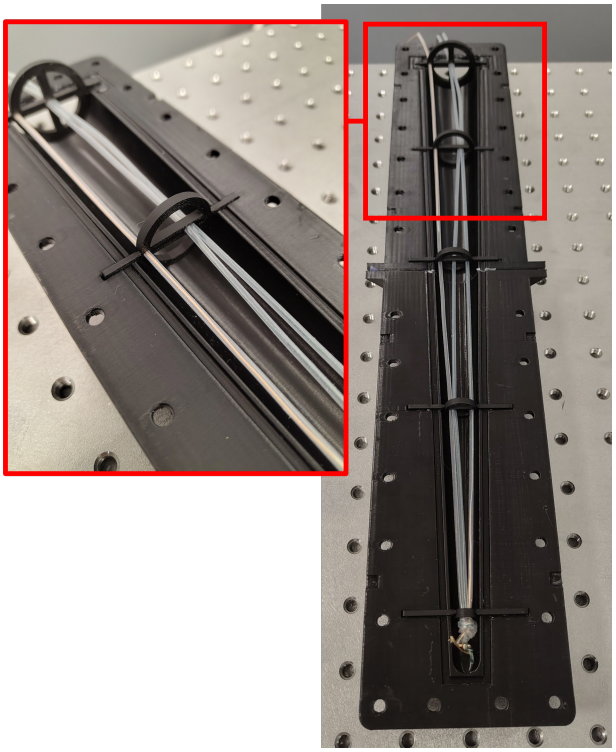

Fig. 20: Mold with linkages and tendons installed, with Close-up of the tendons in their sleeves passing through the 2nd linkage

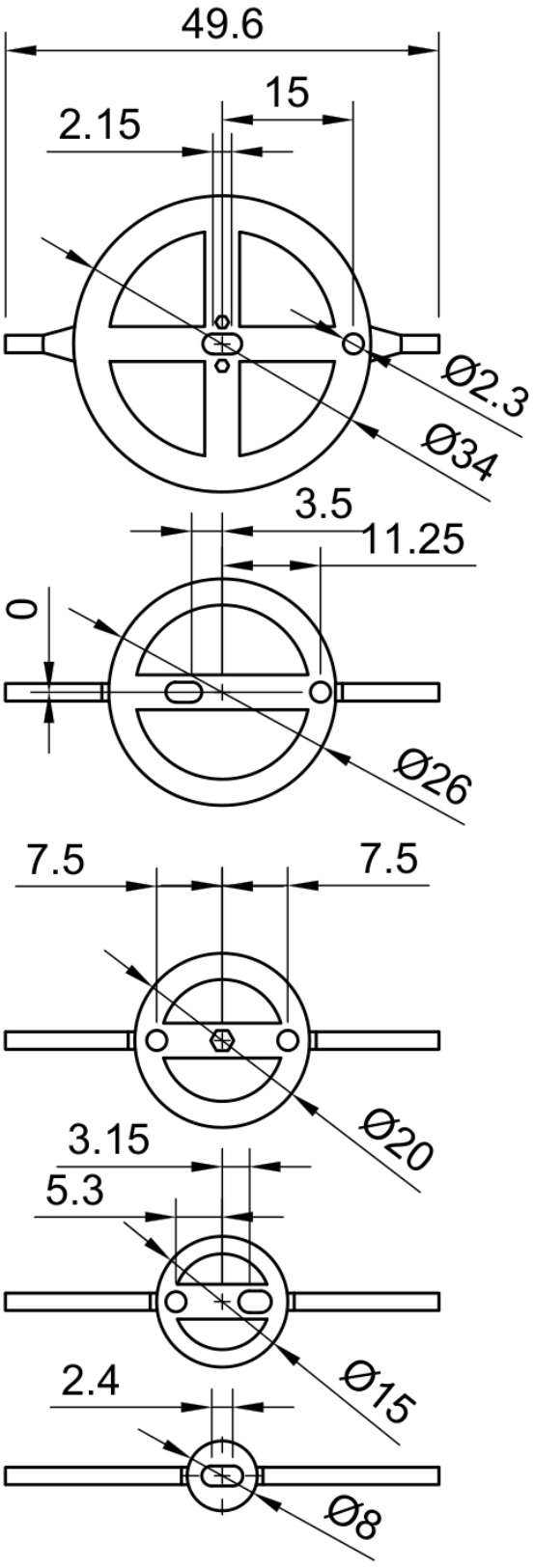

Fig. 21: CAD model of the 5 linkages inside the CSM